Optics Letters

High-power and single-mode VCSEL arrays with single-polarized outputs by using package-induced tensile strain

Jin-Wei Shi,[1,*] Zuhaib Khan,[1] Ray-Hua Horng,[2] Hsiao-Yun Yeh,[2] Chun-Kai Huang,[3] Cheng-Yi Liu,[3] Jie-Chen Shih,[1] Yung-Hao Chang,[1] Jia-Liang Yen,[4] and Jinn-Kong Sheu[5]

[1]Department of Electrical Engineering, National Central University, Jhongli, 320, Taiwan
[2]Institute of Electronics, National Chiao Tung University, Hsinchu 30010, Taiwan
[3]Department of Chemical and Materials Engineering, National Central University, Jhongli, 320, Taiwan
[4]Department of Information Technology, Takming University of Science and Technology, Taipei 114, Taiwan
[5]Department of Photonics, National Cheng Kung University, Tainan City 70101, Taiwan
*Corresponding author: jwshi@ee.ncu.edu.tw

Received 29 May 2020; revised 26 July 2020; accepted 27 July 2020; posted 29 July 2020 (Doc. ID 398896); published 27 August 2020

In this work, we demonstrate a novel high-power vertical-cavity surface-emitting laser (VCSEL) array with highly single-mode (SM) and single-polarized output performance without significantly increasing the intra-cavity loss and threshold current (*I*th). By combining a low-loss zinc-diffusion aperture with an electroplated copper substrate, we can obtain a highly SM output (side mode suppression ratio >50 dB) with a very narrow divergence angle ($1/e^2$: ∼10°) under high output power (3.1 W; 1% duty cycle) and sustain a single polarization state, with a polarization suppression ratio of around 9 dB, under the full range of bias currents. Compared to the reference device without the copper substrate, the demonstrated array can not only switch the output optical spectra from quasi-SM to highly SM but also maintain a close threshold current value (*I*th: 0.8 versus 0.7 mA per unit device) and slope efficiency. The enhancement in fundamental mode selectivity of our VCSEL structure can be attributed to the single-polarized lasing mode induced by tensile strain, which is caused by the electroplated copper substrate, as verified by the double-crystal x-ray measurement results.

https://doi.org/10.1364/OL.398896

High-power vertical-cavity surface-emitting laser (VCSEL) arrays have recently been in great demand due to their applications for 3-dimensional (3-D) sensing [1–3]. Further increasing the brightness of the VCSEL light source has become important because of the sensing distance required for advanced autonomous lidars and surveillance cameras which can range from tens to hundreds of meters [3]. However, most of the commercially available VCSEL arrays exhibit high multi-mode (MM) behaviors with the $1/e^2$ far-field divergence angle at around 25°–30°. One of the most effective ways to significantly enhance the brightness is to build a VCSEL array of single-mode (SM) VCSEL units [4,5]. Several VCSEL structures for attaining higher SM power have been reported, including zinc (Zn)-diffusion [4,5], surface relief [6], photonic crystal [7], and anti-guide (leaky) cavity [8,9] structures. However, it is necessary to incorporate extra intra-cavity loss into these VCSEL structures to suppress the higher-order mode lasing which usually results in an increase in the threshold current (*I*th) and degradation in the quantum efficiency, as compared to those in reference [4–9]. Furthermore, the polarization states of the output from these SM or MM VCSELs are usually not stable under different bias currents [10–12]. In this study, we successfully demonstrate a high-power 940 nm VCSEL array structure, which can attain highly SM and single-polarized output beams without increasing the intra-cavity loss and threshold current. A narrow divergence angle ($1/e^2$: ∼10°), high SM, and a single polarization state can be sustained under the full bias current range with a maximum output power of 3.1 W (1% duty cycle and 5 A bias current). This excellent performance can be attributed to the tensile strain induced by the integration of the electroplated copper substrate, also verified by the double-crystal x-ray measurement results.

Interested readers can refer to our previous work for details of the epi-layer structure and fabrication processes of the VCSEL array [4,5]. Enhancement of the speed and power performance has been reported for the VCSEL structure with electroplated thick copper layers [13]. Here, the electroplating process is performed to grow a copper substrate around 150 μm in thickness on the n-metal contact (backside) of the sample, which has 150 μm thick n^+ GaAs substrate (after lapping) and 8 μm thick active VCSEL cavity layers. Figures 1(a)–1(c) show top views of the demonstrated single reference VCSEL and VCSEL array and a conceptual cross-sectional view of the VCSEL unit, respectively. The mesa size (*W*) and the spacing between neighboring VCSEL units (*D*) in the 1 × 3 column are the same as

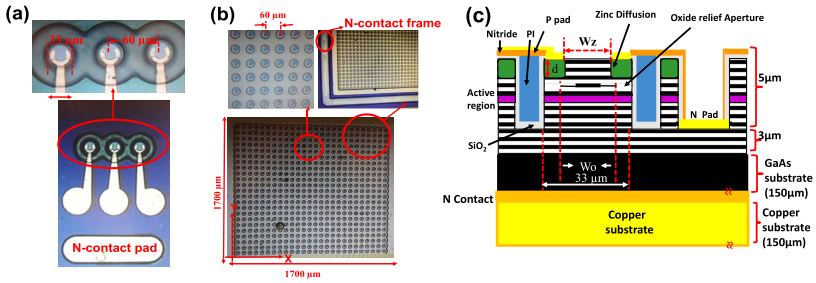

Fig. 1. Top-view of the (a) single reference VCSEL unit, (b) VCSEL array, and (c) conceptual cross-sectional view of the VCSEL unit in the demonstrated array ($W_o/W_Z/d$: 9.5/7.5/1.7 μm). For clearness, (c) is not drawn to scale.

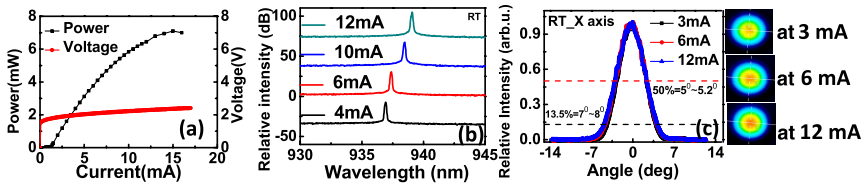

Fig. 2. (a) Measured CW L-I-V curve, (b) optical spectra, and (c) 2-D/1-D far-field patterns of a single-mode reference VCSEL unit at different CW bias currents ($W_o/W_Z/d$: 10.5/7.5/1.7 μm).

those of the VCSEL unit in the array, which has a W and D of 33 and 60 μm, respectively. The total number of light emission apertures in our array is around 570 with a $1.7 \times 1.7\ \mathrm{mm}^2$ active area. The x- and y-axes in Fig. 1(b) are defined for 1-dimensional (1-D) far-field pattern (FFPs) measurement, which will be discussed later. The three key parameters: W_Z, W_O, and d, shown in Fig. 1(c), determine the mode characteristics of the single device. Here, W_Z and W_O represent the diameter of the Zn-diffusion and oxide-confined aperture, respectively; d is the Zn-diffusion depth. By properly optimizing the relative sizes of these three parameters, the device is able to achieve high SM performance under the full range of bias currents in a 10 × 10 VCSEL array [4] at the expense of a significant increase in the threshold current due to the increase of internal loss (α_i.). Figure 2(a) shows the measured light output power (L) versus bias currents (I) and voltage (L-I-V) curves of a single VCSEL fabricated with the same epi-layer structure under continuous wave (CW) operation, producing highly SM performance at the full range of bias currents. Figures 2(b) and 2(c) show the bias dependent output optical spectra and 1-D (x-axis)/2-D FFPs of such a device under room temperature (RT) and CW operation. As can be seen, although we can obtain nice FFPs with a narrow divergence angle ($1/e^2$: ~8°), the required threshold current (Ith) must be greater than 1.3 mA. This should result in a further increase of the operation current in our large array. We thus choose a single device structure ($W_o = 9.5$ μm) with quasi-SM performance and a moderate Ith value (~0.7 mA) when assembling the array. The aperture size values for quasi-SM ($W_o/W_Z/d$: 9.5/7.5/1.7 μm) and high SM ($W_o/W_Z/d$: 10.5/7.5/1.7 μm) devices are specified in the captions of Figs. 1 and 2, respectively. Now, we compare the performance of our quasi-SM VCSEL array after (array A) and before (array B) performing the electroplating process for integration of the additional copper substrate. Figure 3(a) shows the I-V curves of arrays A and B measured under pulse mode (PM) operation (1% duty cycle). Here, the current pulses, which are generated from the

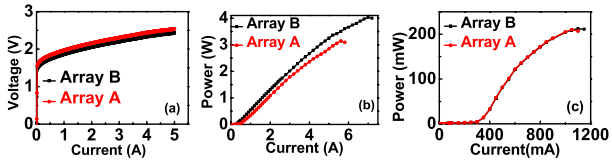

Fig. 3. (a) Measured PM (1% duty cycle) I-V curves of arrays A and B. Measured L-I curves under (b) PM (1% duty cycle) and (c) CW operation.

pulse current source (KEITHLEY 2461) have a 1 ms pulse-width and a tunable duty cycle. The different values of duty cycle for each measurement are specified in the figure caption. We can clearly see that both arrays exhibit similar diode-like I-V characteristics, which clearly indicates that the additional electroplating process does not cause any degradation in the performance of our VCSELs. Figures 3(b) and 3(c) show the measured L versus I under PM and CW operation, respectively. As can be seen, under CW operation, these two arrays (A and B) exhibit the same L-I performance with the same threshold current (Ith) at around 0.3 A. On the other hand, under PM operation, array A exhibits a slightly larger Ith (0.45 versus 0.38 A), less maximum output power (3.1 W versus 4 W), but the same slope efficiency. The large difference in L-I characteristics between CW and PM operation can be attributed to the significant thermal effect that occurs in such large scale arrays (570 units) under CW operation, which becomes the major bottleneck to static performance in both structures. Figures 4(a) and 4(b) show the bias dependent optical spectra measured at different positions (A to E) for arrays A and B, respectively, under PM operation. Here, in order to exclude the significant thermal-induced red shift in lasing wavelengths of array A, which will be discussed in detail later, array A has a smaller driving current pulse duty cycle than array B (0.2% versus 1%) during optical spectra measurement. During measurement, a multi-mode fiber (MMF) with a ball lens tip is used to collect

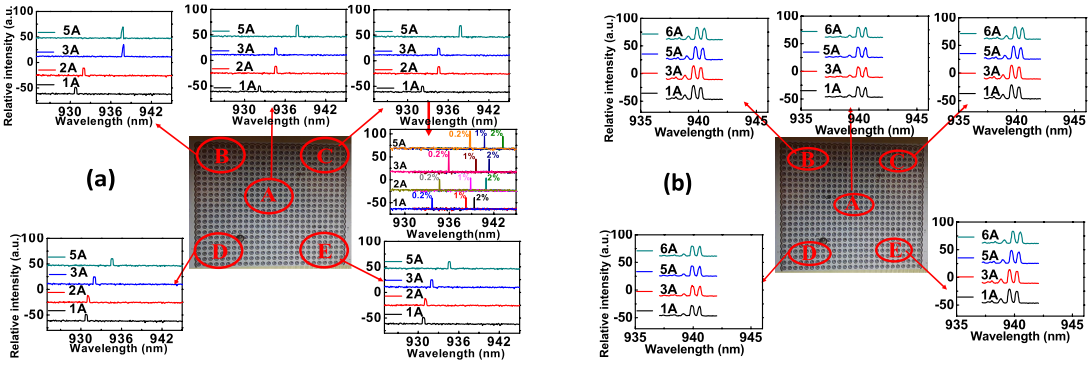

Fig. 4. Bias dependent optical spectra measured at different positions on (a) array A and (b) array B under PM (A: 0.2%; B: 1%) operation. The inset to (a) shows the bias dependent spectra measured under different duty cycles.

the light output from different locations on the array. We can clearly see that after the integration of copper substrate units into the VCSEL array, the output optical spectra from the whole active area show significant switching from quasi-SM to highly SM, with a side mode suppression ratio (SMSR) of over 50 dB, from near the threshold up to the saturation output. Here, the optical transverse side-modes are too weak to be detected by our optical spectrum analyzer (ANDO 6315 A), which has a limited dynamic range and wavelength resolution. In addition, as compared to the spectra of array B, there is a significant blue shift in the lasing wavelength of array A under a low bias current (1 A). This can be attributed to the significant tensile strain induced by the additional copper substrate. The tensile strain results in a thinning of the thickness of the cavity layer and a blue shift of the lasing wavelength can thus be observed (938 nm to 932 nm). The package-induced strain will be discussed in greater detail later. On the other hand, when the bias current increases, array A exhibits a more pronounced red shift in the lasing wavelength than that of array B. Such a phenomenon can be attributed to the large difference in the thermal expansion coefficients of the remaining GaAs and copper layers in the composite substrate of array A. This, in turn, leads to a significant change in the strain, cavity layer thickness, and lasing wavelengths when the bias current (junction temperature) increases. The inset to Fig. 4(a) shows the bias dependent spectra for array A measured at different pulse current duty cycles (0.2%, 1%, and 2%). As can be seen, highly SM performance can be sustained under such a wide operation window, and the expected significant red shift happens when the duty cycles (junction temperature) increases. Figures 5 and 6 show the measured 1-D and 2-D far-field patterns of arrays A and B under PM operation (same duty cycle as 1%) but different bias currents. We can clearly see that in contrast to array A, the Gaussian-like FFPs of array B can be sustained only when the bias current is less than 3 A. The FFP starts to become doughnut-like with a shallow dip (<20%) in the center of the pattern when the bias current is higher. On the other hand, device A exhibits a perfect Gaussian-like FFP with an extremely narrow divergence angle ($1/e^2$: <10°) under the full range of bias currents, which reflects its excellent SM performance, as shown in Fig. 4. From to the measured L-I curves of both arrays (A and B), as shown in Fig. 3, we can understand that the highly SM performance in array A is at the expense of a slightly larger Ith (0.8 versus 0.7 mA) in each unit device than for array B Nevertheless, compared with the highly SM reference sample fabricated only using the Zn-diffusion process, Fig. 2, the unit device in array A can have a much lower Ith (0.8 versus 1.3 mA), and the same highly SM characteristics. In addition, the degradation in the maximum output power per unit device which occurs in array A can be attributed to the spatial hole burning effect [14] induced by the higher power density in the center of its Gaussian mode. Such a significant transition in the output optical mode spectra can be attributed to the significant stress induced over the large active area in our VCSEL array by the addition of the electroplated copper substrate. Figures 6(a) and 6(b) show the double-crystal x-ray (DCXR) measurement results for arrays B and A, respectively. Figure 6(c) shows the measurement results for the bulk GaAs wafer for reference (31.62°). As can be seen, compared with the array B, the diffraction peak of the fabricated array A shifts from 31.43° to 31.68°. Such a shift indicates that the integration of the electroplated copper substrate in array A pushes the internal strain shifts from compressive (array B) to tensile (array A). Using Eq. (1) and the measured diffraction angles, we can then obtain the change of lattice constant in the direction of epi-growth [15] of our array before (5.42×10^{-3}) and after (-1.69×10^{-3}) integration of the copper substrate:

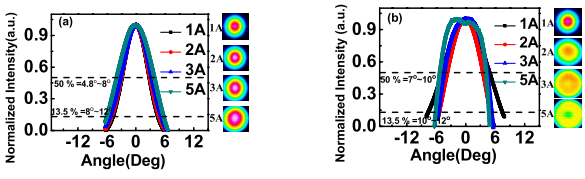

Fig. 5. One-dimensional (in the x-direction) and 2-D far-field patterns measured under different pulse bias currents (1 to 5 A; 1% duty cycle) of (a) array A and (b) array B.

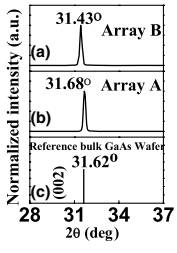

Fig. 6. Measured double x-ray traces of (a) array B, (b) array A, and (c) reference bulk GaAs wafers.

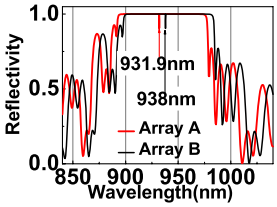

Fig. 7. Simulated VCSEL reflectivity spectra of arrays A and B.

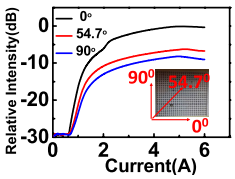

Fig. 8. Measured L-I curves (1% duty cycle) at different orientations (0°: ⟨110⟩, 90°: ⟨1$\bar{1}$0⟩, and 54.7°: ⟨111⟩) with polarizer.

$$\left(\frac{\Delta a}{a}\right)\perp = \frac{\sin\theta_s}{\sin\theta_i} - 1. \quad (1)$$

Here, a is the lattice constant of the bulk GaAs wafer, Δa is the amount of change in the GaAs lattice constant in the vertical direction, and θ_l and θ_s are the measured diffraction angles of the epi-layer and the substrate, respectively. The positive and negative signs represent that the lattice constant is larger or smaller than that of the reference GaAs substrate, respectively. We can see that there is around 0.71% thinning of the epitaxial layers after integration of the copper substrate. With this information, we simulate the VCSEL reflectivity spectra based on the ABCD matrix before and after performing the electroplating process, as shown in Fig. 7 [16]. We can clearly see that the etalon dip (lasing wavelength) shifts from 938 nm to 932 nm, which is pretty consistent with the observed blue shift (938 nm to 932 nm) in our measured optical spectra, as shown in Fig. 4. The polarization states of most of the reported VCSELs hop between two orthogonal orientations (⟨110⟩ and ⟨1$\bar{1}$0⟩) with the change of bias current [10–12]. Figure 8 shows the L-I curve of array A measured under different polarization states obtained by using a polarizer. We can clearly see that array A exhibits stable polarization states along the ⟨110⟩ orientation under the full range of bias currents, producing a polarization suppression ratio (⟨110⟩ versus ⟨1$\bar{1}$0⟩) of around 9 dB, which is much larger than that of SM reference (<1 dB), as discussed in Fig. 2, without copper substrate induced tensile strain. Here, we define the ratio between such two orientations as due to the fact that they are perpendicular to each other and on the same plane (⟨001⟩). The enhancement of transverse mode discrimination in the Zn-diffused aperture of array A can be understood as follows:

The existence of high-order transverse modes usually accompanies the higher-order polarization states so that the single fundamental polarization state lasing in our array A can further increase the loss of higher-order modes, thereby enhancing the selectivity of the fundamental lasing mode [11]. In summary, by combining low-loss Zn-diffusion apertures with tensile strain induced by the electroplating of a copper substrate, we can produce VCSEL arrays characterized by low Ith, high SM, FFPs with very narrow divergence angles, high available power, and single fundamental polarization state output beam. The demonstrated VCSEL array opens up new possibilities for further enhancing the maximum ranging distance of time-of-flight sensing systems at the 940 nm wavelength.

Funding. Ministry of Science and Technology, Taiwan (108-2622-E-008-011-CC2, 109-3116-F-008 -007 -).

Disclosures. Jin-Wei Shi (P) is named as inventor on U.S. provisional patent application 63/016,328 regarding the technology reported in this Letter.

REFERENCES

1. J. Skidmore, Opt. Photon. News **30**, 28 (2019).
2. J.-F. Seurin, C.-L. Ghosh, V. Khalfin, A. Miglo, G. Xu, J. D. Wynn, P. Pradhan, and L. A. D'Asaro, Proc. SPIE **6908**, 690808 (2008).
3. R. F. Carson, M. E. Warren, P. Dacha, T. Wilcox, J. G. Maynard, D. J. Abell, K. J. Otis, and J. A. Lott, Proc. SPIE **9766**, 97660B (2016).
4. J.-L. Yen, K.-L. Chi, J.-W. Jiang, Y.-J. Yang, and J.-W. Shi, IEEE J. Quantum Electron. **50**, 787 (2014).
5. Z. Khan, J.-C. Shih, R.-L. Chao, T.-L. Tsai, H.-C. Wang, G.-W. Fan, Y.-C. Lin, and J.-W. Shi, Optica **7**, 267 (2020).
6. A. Haglund, J. S. Gustavsson, J. Vukusic, P. Modh, and A. Larsson, IEEE Photon. Technol. Lett. **16**, 368 (2004).
7. D. F. Siriani and K. D. Choquette, IEEE Photon. Technol. Lett. **23**, 167 (2011).
8. L. Bao, N.-H. Kim, L. J. Mawst, N. N. Elkin, V. N. Troshchieva, D. V. Vysotsky, and A. P. Napartovich, Appl. Phys. Lett. **84**, 320 (2004).
9. N. N. Ledentsov, V. A. Shchukin, V. P. Kalosha, N. N. Ledentsov, J.-R. Kropp, M. Agustin, L. Chorchos, G. Stepniak, and J. P. Turkiewicz, Opt. Express **26**, 445 (2018).
10. J. M. Osterman and R. Michalzik, *VCSELs: Fundamentals, Technology and Applications of Vertical-Cavity Surface- Emitting Lasers* (Springer, 2013), Vol. **166**.
11. K. D. Choquette and R. E. Leibenguth, IEEE Photon. Technol. Lett. **6**, 40 (1994).
12. E. Haglund, M. Jahed, J. S. Gustavsson, A. Larsson, J. Goyvaerts, R. Baets, G. Roelkens, M. Rensing, and P. O. Brien, Opt. Express **27**, 18892 (2019).
13. A. N. Al-Omari and K. L. Lear, IEEE Photon. Technol. Lett. **17**, 1767 (2005).
14. J.-W. Shi, Z.-R. Wei, K.-L. Chi, J.-W. Jiang, J.-M. Wun, I.-C. Lu, J. Chen, and Y.-J. Yang, J. Lightwave Technol. **31**, 4037 (2013).
15. P. Kidd, J. Mater. Sci.: Mater. Electron. **14**, 541 (2003).
16. L. A. Coldren, S. W. Corzine, and M. L. Mašanović, *Diode Lasers and Photonic Integrated Circuits*, 2nd ed. (Wiley, 2012).